



# TiO<sub>2</sub>/C nanocomposites prepared by thermal annealing of titanium glycerolate as anode materials for lithium-ion batteries

G. S. Zakharova<sup>1</sup> , A. Ottmann<sup>2,\*</sup> , L. Möller<sup>2</sup> , E. I. Andreikov<sup>3</sup> , Z. A. Fattakhova<sup>1,4</sup> ,  
I. S. Puzyrev<sup>3,4</sup> , Q. Zhu<sup>5</sup> , E. Thauer<sup>2</sup> , and R. Klingeler<sup>2,6</sup>

<sup>1</sup>Institute of Solid State Chemistry, Ural Branch of Russian Academy of Sciences, 91 Pervomaiskaya St., Yekaterinburg, Russia 620990

<sup>2</sup>Kirchhoff Institute of Physics, Heidelberg University, INF 227, 69120 Heidelberg, Germany

<sup>3</sup>Postovsky Institute of Organic Synthesis, Ural Branch of Russian Academy of Sciences, 22 Kovalevskoy St., Yekaterinburg, Russia 620990

<sup>4</sup>Ural Federal University, 19 Mira St., Yekaterinburg, Russia 620002

<sup>5</sup>Institute of Materials Science and Engineering, Wuhan University of Technology, Wuhan 430070, People's Republic of China

<sup>6</sup>Centre for Advanced Materials, Heidelberg University, INF 225, 69120 Heidelberg, Germany

Received: 28 February 2018

Accepted: 22 May 2018

Published online:

29 May 2018

© Springer Science+Business Media, LLC, part of Springer Nature 2018

## ABSTRACT

TiO<sub>2</sub>/C nanocomposites have been synthesized by developing a facile route based on the annealing of titanium glycerolate in inert atmosphere at 250–850 °C. X-ray diffraction studies reveal that the annealing temperature determines the crystal structure of the TiO<sub>2</sub> phase in the compounds, which can be amorphous, anatase, and rutile. In contrast, the nanosized rod-like morphology which to a certain extent is predefined by the titanium glycerolate precursor does not depend on the annealing temperature. The carbon content of the TiO<sub>2</sub>/C composites amounts to 16–29 wt% and shows up, e.g., in the characteristic Raman D and G bands. Anatase-structured TiO<sub>2</sub>/C, which is obtained at 600 °C, exhibits the best electrochemical performance among the studied materials. Without the addition of carbon black, it reaches an initial specific discharge capacity of 378 mA h g<sup>-1</sup> at 100 mA g<sup>-1</sup> and exhibits excellent rate capability with a capacity of 186 mA h g<sup>-1</sup> at 1000 mA g<sup>-1</sup>.

## Introduction

Improving the performance of lithium-ion batteries has become one of the key topics in materials science. The demands for high-performance batteries have

led to extensive research efforts regarding the development of electrode materials featuring high capacity, long lifespan, chemical stability, low cost, and environmental benignity [1, 2]. In this regard, nanosized titanium dioxide (TiO<sub>2</sub>) in the form of its polymorphs anatase [3–5] and rutile [6, 7],

Address correspondence to E-mail: alex.ottmann@kip.uni-heidelberg.de

respectively, or a mixture of these phases [8] has become a promising candidate for application in lithium-ion batteries [9]. In order to enhance the cycling performance and high rate capability of  $\text{TiO}_2$  anode materials, various nanocomposites incorporating conductive carbon allotropes have been formed. For instance, CNTs/ $\text{TiO}_2$  coaxial nanocables synthesized by controlled hydrolysis of tetrabutyl titanate in the presence of carbon nanotubes (CNTs) demonstrate outstanding specific capacities which are three times higher than that of pristine  $\text{TiO}_2$  without CNTs [10]. Owing to the superior electric conductivity and large specific surface area, graphene is also regarded as an ideal component in  $\text{TiO}_2$  nanocomposites [11–13]. Besides the addition of CNTs or graphene, other methods and forms of carbon can be used for the preparation of  $\text{TiO}_2/\text{C}$  nanocomposites with enhanced electrochemical performance. Utilizing the formation of amorphous carbon in situ by carbonization of oleic acid [14], glucose [15], sorbitol [16] or polyvinylpyrrolidone [17, 18] absorbed on the surface of  $\text{TiO}_2$  nanorods, various  $\text{TiO}_2/\text{C}$  composites were produced. Furthermore,  $\text{TiO}_2/\text{C}$  nanocomposites were fabricated by combining carbonization of glucose and hydrolysis of a titanium glycolate precursor by means of hydrothermal treatment [19, 20]. Also, Li et al. [21] synthesized  $\text{TiO}_2/\text{C}$  chrysanthemum-like nanocomposites via carbonization of organic groups of titanium glycolate rods in vacuum at 400 °C.

Most of the existing synthetic methods for the preparation of  $\text{TiO}_2/\text{C}$  nanocomposites are based on the treatment of liquid precursors under hydrothermal conditions [15, 17–19, 22]. A novel approach employs solid-state reactions based on metal alkoxides as a new type of precursor [23]. During this synthesis process, solid metal alkoxides conveniently convert into functional inorganic nanomaterials and nanocomposites, respectively. Thereby, the morphology, chemical composition, and crystal structure of the final product can be controlled by the choice of suitable alkoxide precursors. In this regard, titanium glycolate is a member of the titanium alkoxides family which indeed can be used as precursor for preparing  $\text{TiO}_2$  nanomaterials [24, 25].

Hence, a new synthetic strategy concerning the formation of  $\text{TiO}_2/\text{C}$  nanocomposites can be successfully realized by heat treatment of titanium glycolate (TiGly) under inert atmosphere. The organic component of TiGly will partially transform

into carbon resulting in the formation of a  $\text{TiO}_2/\text{C}$  composite. Therefore, this precursor-controlled synthetic route is very effective and elegant, contributing to the development of advanced  $\text{TiO}_2/\text{C}$  composite materials. Here, we report the application of this method yielding  $\text{TiO}_2/\text{C}$  rod-like nanocomposites, some of which show outstanding electrochemical performance, in particular rate capability, as anode material in Li-ion batteries.

## Experimental

### Materials preparation

Titanium(IV) butoxide (pure grade) and freshly distilled glycerol (analytical grade) were used as starting materials for the synthesis of the titanium glycolate precursor. In a typical procedure, 15 mL of titanium n-butoxide ( $\text{Ti}(\text{OC}_4\text{H}_9)_4$ ) was added to 150 mL of glycerol in a 250-mL round-bottom flask attached to a condenser. The resultant solution was then heated to 190 °C under  $\text{N}_2$  atmosphere for 24 h. After cooling to room temperature, the resulting white precipitate, titanium glycolate, was collected using centrifugation, washed with ethanol and dried at 100 °C for 24 h.

$\text{TiO}_2/\text{C}$  nanocomposites were prepared by annealing the as-obtained titanium glycolate in a tube furnace at different temperatures ranging from 250 to 850 °C for 2 h under  $\text{N}_2$  flow at an initial heating rate of 5 °C/min. A slow heating rate of 5 °C/min was chosen in order to ensure the formation of the composite without destroying the nanofibrillar structure of titanium glycolate. The carbonized products are labeled as  $\text{TiO}_2/\text{C}-X$ , where X is the annealing temperature.

### Materials characterization

X-ray diffraction (XRD) patterns were obtained from a Shimadzu XRD-7000S using  $\text{Cu K}_\alpha$  radiation with a step size of  $\Delta 2\theta = 0.02^\circ$ . The morphology of the powders was investigated on a ZEISS Leo 1530 scanning electron microscope (SEM) and a JEOL JEM 2100 transmission electron microscope (TEM). The Raman spectra of the samples were recorded on a U1000 “Renishaw” spectrometer using a 532 nm laser at the output power of 40 mW. Thermogravimetric analysis (TG/DTA) was performed on a Mettler

Toledo TGA/DSC1 analyzer with a heating rate of 5 °C/min under N<sub>2</sub> flow and in air. Nitrogen sorption isotherms were determined on a Micromeritics Gemini VII 2390 Surface Area Analyzer. Prior to N<sub>2</sub> physisorption data collection, the samples were degassed at 140 °C under vacuum for 2 h. The specific surface area, pore size distribution and pore volumes were obtained by means of the Brunauer–Emmett–Teller (BET) method and the Barrett–Joyner–Halenda (BJH) model from the adsorption branches of the isotherms.

### Electrochemical measurements

For electrochemical characterization, pristine TiO<sub>2</sub>/C-X powder was stirred overnight with 6 wt% polyvinylidene difluoride binder (Solvay Plastics) in N-methyl-2-pyrrolidone (Sigma-Aldrich). The resulting slurry was spread on copper meshes, dried at ~ 80 °C under vacuum, mechanically pressed and dried again. Swagelok-type two-electrode cells were assembled in an Ar-atmosphere glove box [5]. Therein, the working electrode and a lithium metal foil counter electrode were separated by two layers of glass fiber separator (Whatman GF/D). The electrolyte was 1 mol/l LiPF<sub>6</sub> in a mixture of ethylene carbonate and dimethyl carbonate (Merck Electrolyte LP30). Electrochemical measurements by means of cyclic voltammetry and galvanostatic cycling with potential limitation were taken on a VMP3 Potentiostat System (BioLogic) in the potential range of 0.01–3.0 V versus Li/Li<sup>+</sup> at a constant temperature of 25 °C. The accuracy of the quantitative results, e.g., specific capacities, is determined by the error of the mass of active material per electrode, which usually amounts to 5%. This order of relative error is also found as variance comparing independent measurements with the same parameters.

### Results and discussion

The titanium glycolerate (TiGly) precursor which is used for the synthesis of the TiO<sub>2</sub>/C nanocomposite product shows a nanoscale morphology, too, as seen by SEM and TEM images in Fig. 1a, b, respectively. The microscopy images imply that as-prepared TiGly powder is composed of nanorods which are 20–30 nm in diameter and 300–400 nm in length. The surface area is accordingly large and amounts to

47.6 ± 1.7 m<sup>2</sup>/g. Its XRD pattern (Fig. 1c) confirms a phase pure material and the diffraction peaks can be indexed in space group P2/c with the same lattice parameters as reported in Ref. [24]. Investigation of the thermal behavior of TiGly in N<sub>2</sub>-flow gives insight into the precursor transformation during decomposition. The thermal decomposition in inert atmosphere (see Fig. 1d) actually involves three steps which is consistent with published results [24]. A first weight loss of ~ 38.4 wt% occurs step-like and is attributed to the decomposition of TiGly. This process is accompanied by an exothermic feature around 355 °C, indicating the formation of a TiO<sub>2</sub> phase. The weight loss in the temperature range of 357–570 °C (~ 4.5 wt%) corresponds to the evaporation of the remaining organic fragments of TiGly. The final weight loss of ~ 7.1 wt% between 570 and 1000 °C, accompanied by a weak exothermic peak at 960 °C, can be attributed to a carbothermic reaction between TiO<sub>2</sub> and carbon.

The products TiO<sub>2</sub>/C-X produced by the decomposition of TiGly show XRD diffraction patterns which strongly depend on the actual annealing temperature (X). The corresponding XRD patterns are shown in Fig. 2a in comparison with the Bragg positions of an anatase (ICSD #92363 [26]) and a rutile (ICSD #31330 [27]) reference material. The data imply that TiO<sub>2</sub>/C nanocomposites obtained by heat treatment below 480 °C exhibit amorphous phases only. An anatase TiO<sub>2</sub> phase starts to appear after annealing of TiGly at 500 °C. However, the diffraction peaks are broad which can be attributed to nanosized TiO<sub>2</sub> crystallites. In general, TiO<sub>2</sub>/C compounds with anatase structure have been obtained in the range of 500–600 °C. The thermolysis of TiGly at temperatures above 600 °C leads to the formation of rutile TiO<sub>2</sub>, coexisting with the still occurring anatase phase, which is the case in, e.g., TiO<sub>2</sub>/C-600(A + R). However, with annealing in separate heating procedures starting from 400 °C in steps of 50 °C, the sample TiO<sub>2</sub>/C-600(A) without any detectable rutile phase fraction could also be synthesized, at finally 600 °C.

The nitrogen adsorption–desorption isotherms of the samples annealed at 360, 600 and 850 °C (see Fig. 2b) show type IV behavior with H3 hysteresis loops according to the IUPAC classification [28]. The BET specific surface area and the associated pore volumes of the TiO<sub>2</sub>/C-X samples are summarized in Table 1. In contrast to the high-temperature products, the pyrolysis of TiGly below 480 °C yields rather

**Figure 1** Characterization of titanium glycerolate by means of **a** SEM, **b** TEM, **c** XRD, and **d** TG/DTA.

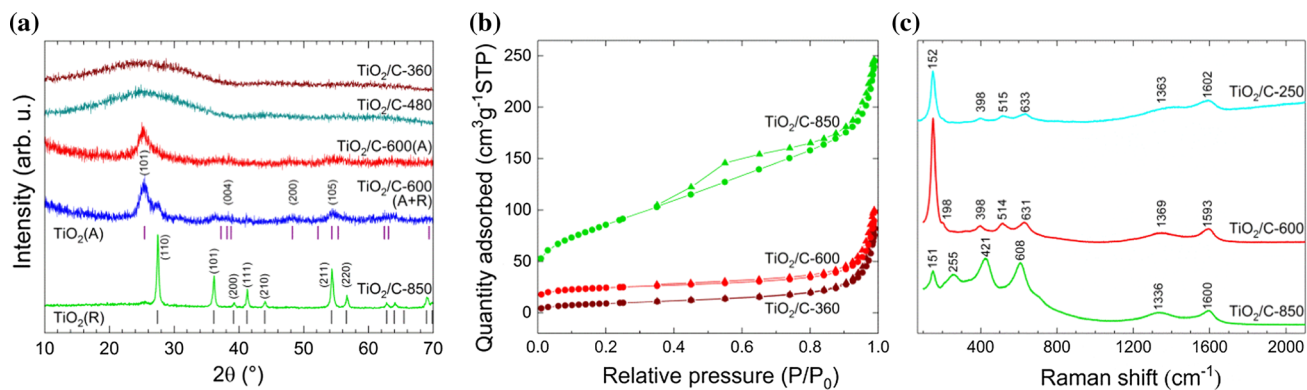
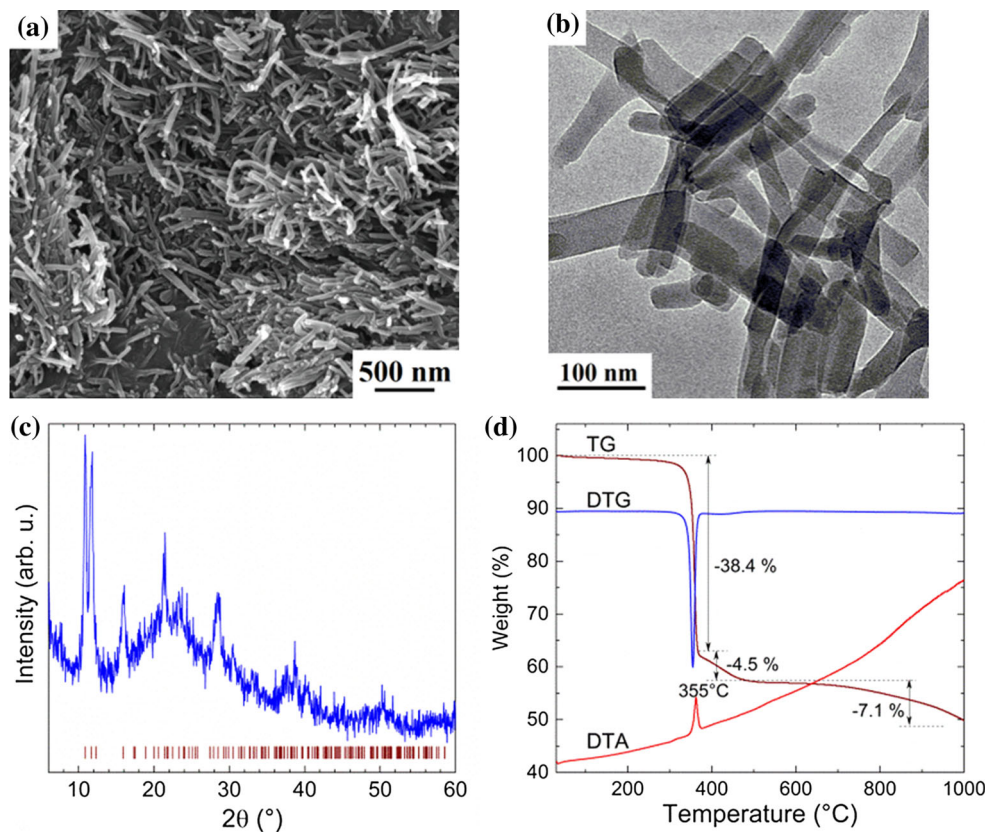


**Figure 2** **a** XRD, **b** BET, and **c** Raman data of  $\text{TiO}_2/\text{C-X}$ . The vertical ticks in **a** show the expected Bragg positions for the anatase (ICSD #92363) and rutile (ICSD #31330) structures.

small surface areas. Increasing the annealing temperature to 600 °C and above affects the textural properties of the  $\text{TiO}_2/\text{C-X}$  samples significantly as, e.g., the specific surface area of the micropores  $S_{\text{micro}}$  increases significantly. This behavior may be explained by the formation of micropores as a result of the anatase crystallization [29]. Further increasing the annealing temperature up to 850 °C leads to a drastic increase in surface area which we attribute to the formation of defects in the composite structure

during the carbothermal reduction of  $\text{TiO}_2$  (cf. Fig. 1d) accompanied by a decrease in the carbon content [29].

The amount of carbon in the  $\text{TiO}_2/\text{C-X}$  nanocomposites as well as its nature is evident from Raman and TG/DTA data. All Raman spectra (Fig. 2c) demonstrate two peaks centered around 1350 and 1600  $\text{cm}^{-1}$ , which can be assigned to the fundamental D and G bands of carbon, related to structurally disordered graphitic domains and graphitic carbon,

**Table 1** Textural properties (i.e., specific surface area  $S_{\text{BET}}$ , micropore volume and respective specific surface area of the micropores  $S_{\text{micro}}$ ) of  $\text{TiO}_2/\text{C-X}$  composites

Samples	$S_{\text{BET}}$ ( $\text{m}^2/\text{g}$ )	$S_{\text{micro}}$ ( $\text{m}^2/\text{g}$ )	Pore volume ( $\text{cm}^3/\text{g}$ )
TiGly	$47.6 \pm 1.7$	–	0.12
$\text{TiO}_2/\text{C-360}$	$33.4 \pm 0.2$	4.5	0.12
$\text{TiO}_2/\text{C-480}$	$30.2 \pm 0.2$	3.2	0.17
$\text{TiO}_2/\text{C-600}$	$78.5 \pm 1.2$	50.2	0.12
$\text{TiO}_2/\text{C-850}$	$305.6 \pm 1.0$	57.2	0.31

respectively. Hence, the results of Raman spectroscopy combined with XRD confirm that the  $\text{TiO}_2/\text{C-X}$  samples are composites of  $\text{TiO}_2$  and carbon. In addition to the D and G bands of carbon, Raman spectra of the composite prepared at 600 °C demonstrate active modes at 152, 198, 398, 514, and 631  $\text{cm}^{-1}$ . These observed vibrational modes agree well with the characteristic peaks of anatase-structured  $\text{TiO}_2$  [30]. While these results agree to the observation of the crystalline anatase structure in the XRD data (see Fig. 2a), the Raman spectrum of  $\text{TiO}_2/\text{C-360}$  shows intense peaks at nearly the same wavenumbers, too. This implies that anatase domains are already formed at an annealing temperature of 360 °C which, however, do not evolve into long-range crystalline order. In the spectrum of  $\text{TiO}_2/\text{C-850}$ , several peaks located at 151, 255, 421, 608  $\text{cm}^{-1}$  are assigned to the vibrational modes of  $\text{TiO}_2$  in the rutile modification [31]. The vibrational modes of this composite with coexisting anatase and rutile structures are shifted toward lower frequencies in comparison with the published data [30, 31], which may be explained by longer Ti–O bond lengths.

The carbon content in the various  $\text{TiO}_2/\text{C-X}$  composites is estimated by thermogravimetric analysis in air. The TGA data show two weight loss steps in the temperature range between 25 and 850 °C. While the initial weight losses below 220 °C are due to the evaporation of adsorbed water, weight changes at higher temperatures are attributed to the combustion of carbon. The latter amount to 29, 26, 26, and 16 wt% for  $\text{TiO}_2/\text{C-360}$ ,  $\text{TiO}_2/\text{C-480}$ ,  $\text{TiO}_2/\text{C-600(A)}$ , and  $\text{TiO}_2/\text{C-850}$ , respectively. Evidently, only the  $\text{TiO}_2/\text{C-850}$  sample exhibits a reduced carbon content (16 wt%), governed by the carbothermal reduction with  $\text{TiO}_2$  which leads to the formation of lower titanium oxides or/and titanium oxycarbide [29, 32].

Typical SEM images of the different  $\text{TiO}_2/\text{C-X}$  samples are displayed in Fig. 3a–d. All

nanocomposites show similar rod-like morphology which does not clearly depend on the temperature of the heat treatment under nitrogen. All SEM images show lots of aggregated rods which are assembled into chrysanthemum-like structures. The individual rods are 3.5–6.5  $\mu\text{m}$  long and 100–250 nm broad, i.e., in both dimensions larger than the rods present in the TiGly precursor. The increase in dimensions may originate from the loss of ligands (OH groups and organic rest) in TiGly as well as its accompanying phase transformation during the thermal annealing. This process can lead to a looser packaging of the rods, making them thicker and longer. A HRTEM image of the  $\text{TiO}_2/\text{C-600(A)}$  composite (Fig. 3e) shows both crystalline and amorphous regions. In detail,  $d$  spacings of 0.238 nm and 0.352 nm, found in crystalline areas, correspond to the (004) and (101) planes in the anatase phase. In this regard, all diffraction rings of a SAED pattern (Fig. 3f) could be indexed ((101), (004), (200), (211), and (204) planes) to polycrystalline anatase  $\text{TiO}_2$  as well. Amorphous layers embedded between the identified crystalline  $\text{TiO}_2$  nanoparticles with a thickness of roughly 3.5 nm may be ascribed to carbon patches (Fig. 3e), further indicating the coexistence of  $\text{TiO}_2$  crystallites and carbon in the nanocomposites.

The electrochemical performance of two samples,  $\text{TiO}_2/\text{C-600(A)}$  and  $\text{TiO}_2/\text{C-600(A + R)}$ , both annealed at 600 °C but only  $\text{TiO}_2/\text{C-600(A + R)}$  containing a significant fraction of rutile phase (cf. Figure 2a), was evaluated by means of cyclic voltammetry and galvanostatic cycling in the potential range of 0.01–3.0 V versus Li/Li<sup>+</sup>. The extended potential range was selected in order to make use of the lithium storage capability of the incorporated carbon in the  $\text{TiO}_2/\text{C-600}$  nanocomposites. Due to the presence of embedded carbon in the nanocomposites under study, no additional carbon black was necessary to prepare mechanically stable and electrochemically active electrodes.

Cyclic voltammograms (CV) of the 1st, 2nd and 10th cycles, measured at a scan rate of 0.1  $\text{mV s}^{-1}$ , are compared in Fig. 4. Both samples exhibit a red/ox peak pair around 1.7/2.05 V which is characteristic for the intercalation/deintercalation of Li<sup>+</sup>-ions into anatase  $\text{TiO}_2$  [33–35]. During the initial cathodic scan, the  $\text{TiO}_2/\text{C-600(A + R)}$  compound (Fig. 4b) additionally shows two irreversible reduction peaks at 1.05 V and 1.38 V, associated with lithiation effects on rutile  $\text{TiO}_2$  [36, 37]. At the same voltages, small

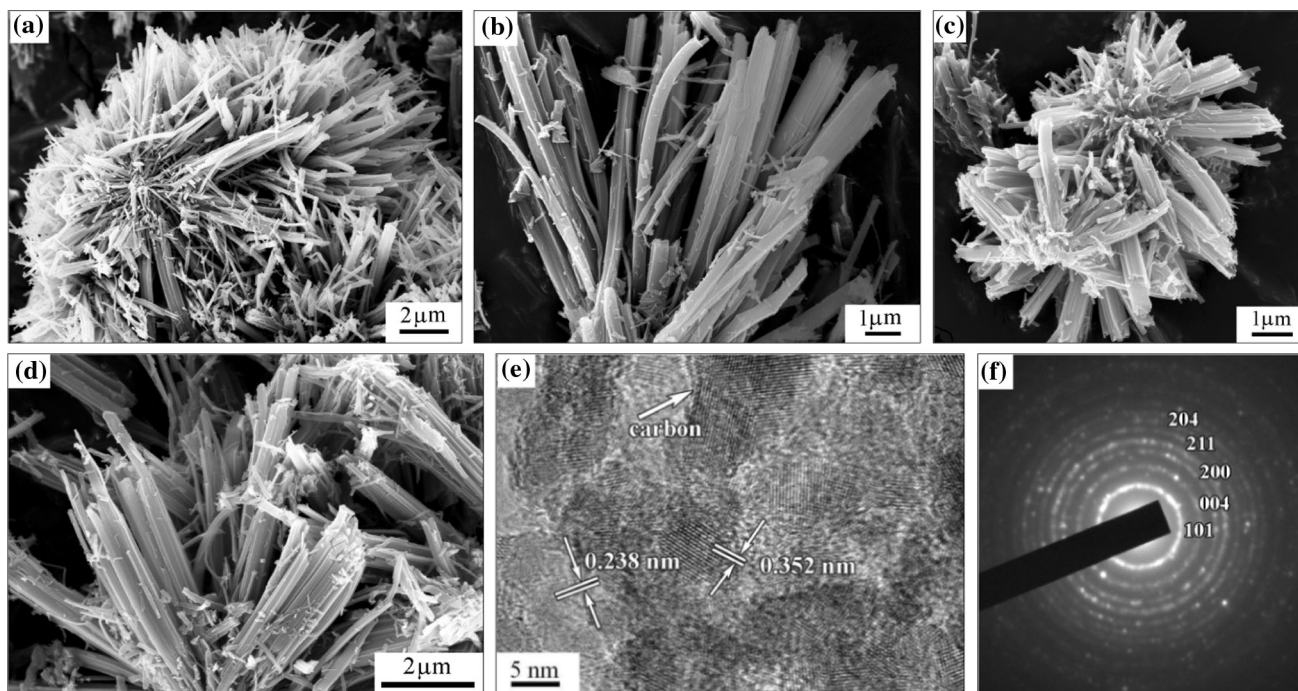


**Figure 3** SEM images of TiO<sub>2</sub>/C-X composites produced at various temperatures: **a** 360 °C, **b** 480 °C, **c** 600 °C, **d** 850 °C, and **e** HRTEM image with **f** the corresponding selected area electron diffraction of TiO<sub>2</sub>/C-600.

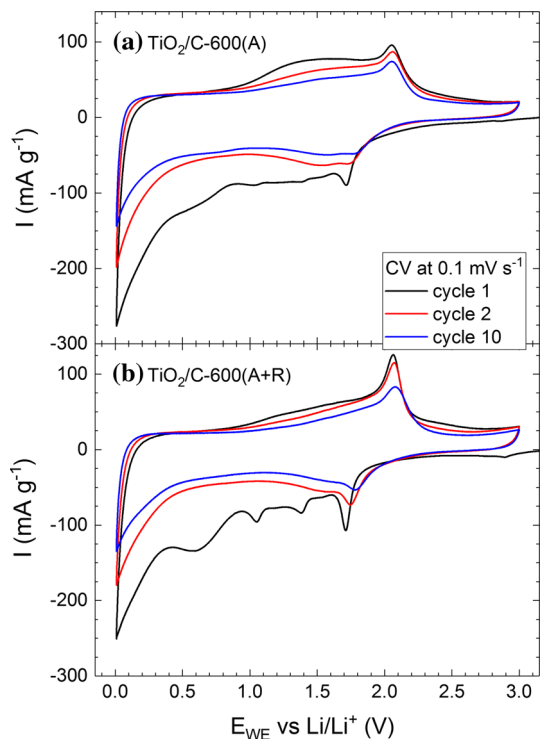


**Figure 4** Cyclic voltammograms of TiO<sub>2</sub>/C-600 at 0.1 mV s<sup>-1</sup>. The material (A) mainly consists of anatase while (A + R) in addition shows rutile in the XRD patterns.

reductive features occur in case of the TiO<sub>2</sub>/C-600(A) compound, which may point to a small rutile phase fraction which is not detectable by means of XRD. The formation of a solid electrolyte interphase (SEI), facilitated by the presence of carbon in the TiO<sub>2</sub>/C-600 composites, is indicated by an irreversible reductive feature around 0.6 V in the initial half cycles [38]. The lithiation of this carbon component is demonstrated by a distinct reduction peak at 0.01 V in all cycles [39]. Further non-peak-like red/ox activity, roughly 0.5–1.5 V/0.8–1.8 V, which appears more pronounced in the case of TiO<sub>2</sub>/C-600(A), can be ascribed to surface-related storage processes [40, 41], supported by the big interfacial area of the TiO<sub>2</sub>/C nanocomposites [42, 43]. Both investigated samples suffer considerable irreversibility, illustrated by strongly decreasing peak intensities during the ten displayed CV cycles.

Galvanostatic cycling with potential limitation (GCPL) provides further information on the cycling stability. The data have been obtained at a specific dis-/charge current of 100 mA g<sup>-1</sup>. The resultant dis-/charge capacities over the course of 100 cycles (a) and corresponding voltage profiles (b) are displayed in Fig. 5. The latter coincide with the observations of the CVs: exemplarily, plateau-like regions

around 1.7 V during charge, i.e., lithiation, and 2.0 V during discharge indicate lithium intercalation and deintercalation, respectively, of anatase  $\text{TiO}_2$ . Flattening charge profiles nearing 0.01 V correspond to the lithiation of carbon in the  $\text{TiO}_2/\text{C-600}$  composites. The observed initial charge and discharge capacities of 698/378 and 745/396  $\text{mA h g}^{-1}$  for  $\text{TiO}_2/\text{C-600(A)}$  and  $\text{TiO}_2/\text{C-600(A + R)}$ , respectively, show strong irreversible contributions, which can be partly attributed to the SEI formation. Pronounced capacity losses with coulombic efficiencies below 95% persist for several cycles in case of both samples. However, the  $\text{TiO}_2/\text{C-600(A)}$  electrode stabilizes way better than the  $\text{TiO}_2/\text{C-600(A + R)}$  one, exhibiting higher discharge capacities from cycle 21 (273  $\text{mA h g}^{-1}$ ) on with a subsequent capacity retention of 82% until cycle 100 (225  $\text{mA h g}^{-1}$ ). The superior cycling stability of  $\text{TiO}_2/\text{C-600(A)}$  in comparison with  $\text{TiO}_2/\text{C-600(A + R)}$  can be ascribed to the irreversibility of the lithiation processes of rutile  $\text{TiO}_2$ , as described,

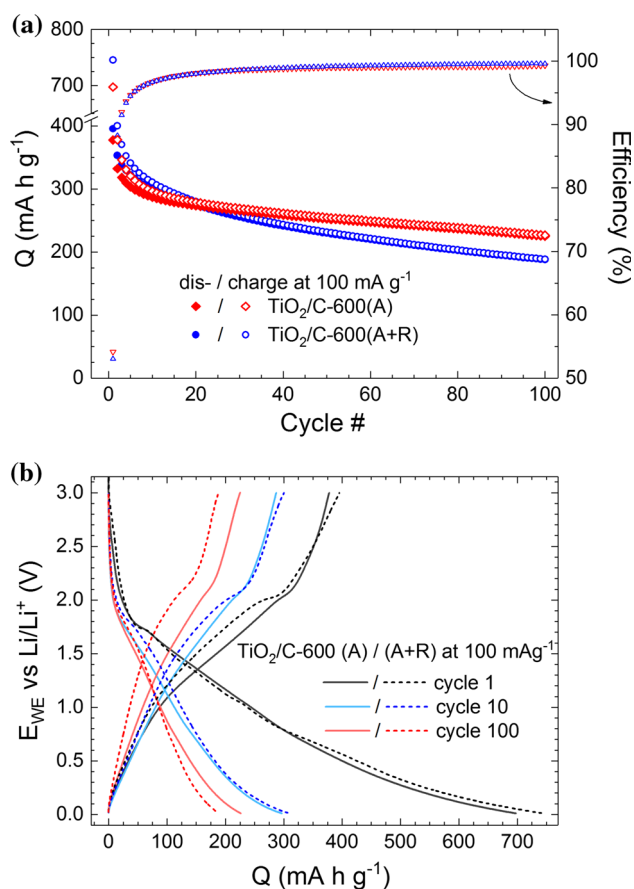


**Figure 5** **a** Specific capacities of  $\text{TiO}_2/\text{C-600(A)}$  and  $\text{TiO}_2/\text{C-600(A + R)}$  at  $100 \text{ mA g}^{-1}$ , and **b** corresponding voltage profiles.

e.g., in [37]. Besides an immediate capacity loss, this also yields electrochemically inactive patches in the nanocomposite material, compromising the long-term stability and conductivity of the  $\text{TiO}_2/\text{C}$  network.

The results are confirmed by the rate capability data with consecutive GCPLs at 100, 250, 500, 1000, and again  $100 \text{ mA g}^{-1}$  for 10 cycles each (Fig. 6). Overall, the  $\text{TiO}_2/\text{C-600(A)}$  compound features the better stability with a capacity retention of 95% between cycle 10 (294  $\text{mA h g}^{-1}$ ) and 42 (279  $\text{mA h g}^{-1}$ ), both at  $100 \text{ mA g}^{-1}$ , as well as the better rate capability with discharge capacities as high as 226  $\text{mA h g}^{-1}$  at  $500 \text{ mA g}^{-1}$  and 186  $\text{mA h g}^{-1}$  at  $1000 \text{ mA g}^{-1}$ . The fact that the specific capacities of the  $\text{TiO}_2/\text{C-600(A + R)}$  sample drop more significantly upon increasing the current, for instance 22% as compared to 16% for  $\text{TiO}_2/\text{C-600(A)}$  from 500 to  $1000 \text{ mA g}^{-1}$ , supports the scenario of compromised synergetic properties, i.e., enhanced conductivity, of the  $\text{TiO}_2/\text{C}$  composites, introduced by inactive, initially rutile patches. The specific capacities, in particular the rate capability, of the  $\text{TiO}_2/\text{C-600(A)}$  nanocomposite competes well with other publications both on  $\text{TiO}_2$  nanomaterials [5, 44] and various  $\text{TiO}_2/\text{C}$  composites [11, 42, 45–47], as summarized in Table S1. This shows that the facile synthesis approach, annealing TiGly under protective atmosphere, yields hybrid  $\text{TiO}_2/\text{C}$  nanocomposites which can be utilized as anode materials in Li-ion batteries. Therefore, a specific benefit of the incorporated carbon is the enhanced conductivity of carbon composites compared to pure  $\text{TiO}_2$  electrode materials, as quantified by several  $\text{TiO}_2/\text{C}$  composite studies [11, 42, 45–47].

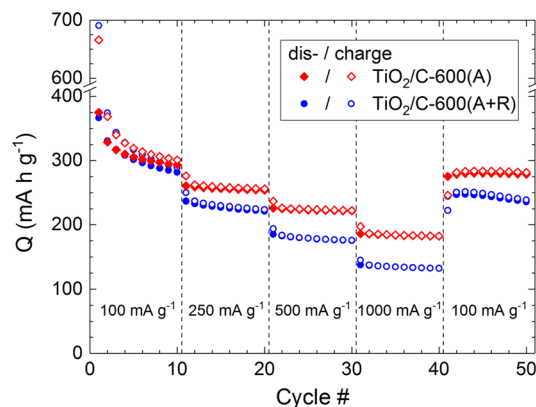


**Figure 6** Rate capability of  $\text{TiO}_2/\text{C-600(A)/(A + R)}$  at 100, 250, 500, and  $1000 \text{ mA g}^{-1}$ .

## Conclusions

A series of TiO<sub>2</sub>/C nanocomposites was synthesized via the annealing of titanium glycerolate in inert atmosphere. The annealing temperature enables controlling the crystal structure, i.e., the presence of amorphous, anatase, and/or rutile TiO<sub>2</sub>. It also strongly affects the surface area and the porosity of the material. The coexistence of TiO<sub>2</sub> and C is verified by means of Raman spectroscopy, TEM, and thermogravimetric analysis, which shows carbon contents of 16–29 wt%. Electrochemical characterization of TiO<sub>2</sub>/C-600 electrodes which were prepared without additional carbon black by means of cyclic voltammetry shows characteristic red/ox activity for the constituents carbon, and anatase and rutile TiO<sub>2</sub>. Galvanostatic charge/discharge at currents up to 1000 mA g<sup>-1</sup> shows that anatase TiO<sub>2</sub>/C-600(A) exhibits excellent rate capability and better cycling stability compared to rutile containing TiO<sub>2</sub>/C-600(A + R).

## Acknowledgements

This work was supported by the CleanTech-Initiative of the Baden-Württemberg-Stiftung (project CT3 Nanostorage). G.S.Z acknowledges support by the Excellence Initiative of the German Federal Government. A.O. acknowledges support by the IMPRS-QD. Q.Z. acknowledges support by the National Natural Science Foundation of China (Projects 51611130056 and 51472189). The authors thank I. Glass for experimental support.

**Data availability statement** The datasets generated during and/or analyzed during the current study are available from the corresponding author on reasonable request.

## Compliance with ethical standards

**Conflict of interest** The authors declare that they have no conflict of interest.

**Electronic supplementary material:** The online version of this article (<https://doi.org/10.1007/s10853-018-2488-9>) contains supplementary material, which is available to authorized users.

## References

- [1] Scrosati B, Garche J (2010) Lithium batteries: status, prospects and future. *J Power Sources* 195(9):2419–2430
- [2] Su X, Wu Q, Zhan X et al (2012) Advanced titania nanostructures and composites for lithium ion battery. *J Mater Sci* 47(6):2519–2534. <https://doi.org/10.1007/s10853-011-5974-x>
- [3] Xu J, Jia C, Cao B et al (2007) Electrochemical properties of anatase TiO<sub>2</sub> nanotubes as an anode material for lithium-ion batteries. *Electrochim Acta* 52(28):8044–8047
- [4] Wu F, Li X, Wang Z et al (2011) A novel method to synthesize anatase TiO<sub>2</sub> nanowires as an anode material for lithium-ion batteries. *J Alloys Compd* 509(8):3711–3715
- [5] Zakharova GS, Jähne C, Popa A et al (2012) Anatase Nanotubes as an Electrode Material for Lithium-Ion Batteries. *J Phys Chem C* 116(15):8714–8720
- [6] Pfanzelt M, Kubiak P, Fleischhammer M et al (2011) TiO<sub>2</sub> rutile—an alternative anode material for safe lithium-ion batteries. *J Power Sources* 196(16):6815–6821
- [7] Fei H, Wei M (2011) Facile synthesis of hierarchical nanostructured rutile titania for lithium-ion battery. *Electrochim Acta* 56(20):6997–7004
- [8] Han X, Han X, Sun L et al (2016) Facile preparation of hybrid anatase/rutile TiO<sub>2</sub> nanorods with exposed (010) facets for lithium ion batteries. *Mater Chem Phys* 171:11–15
- [9] Deng D, Kim MG, Lee JY et al (2009) Green energy storage materials: nanostructured TiO<sub>2</sub> and Sn-based anodes for lithium-ion batteries. *Energy Environ Sci* 2(8):818–837
- [10] Cao F-F, Guo Y-G, Zheng S-F et al (2010) Symbiotic coaxial nanocables: facile synthesis and an efficient and elegant morphological solution to the lithium storage problem. *Chem Mater* 22(5):1908–1914
- [11] Cai D, Lian P, Zhu X et al (2012) High specific capacity of TiO<sub>2</sub>-graphene nanocomposite as an anode material for lithium-ion batteries in an enlarged potential window. *Electrochim Acta* 74:65–72
- [12] Wang D, Choi D, Li J et al (2009) Self-assembled TiO<sub>2</sub>-graphene hybrid nanostructures for enhanced Li-ion insertion. *ACS Nano* 3(4):907–914
- [13] Li N, Zhou G, Fang R et al (2013) TiO<sub>2</sub>/graphene sandwich paper as an anisotropic electrode for high rate lithium ion batteries. *Nanoscale* 5(17):7780–7784
- [14] Ren Z, Chen C, Fu X et al (2014) TiO<sub>2</sub>/C composites nanorods synthesized by internal-reflux method for lithium-ion battery anode materials. *Mater Lett* 117:124–127
- [15] Yang Z, Du G, Guo Z et al (2011) TiO<sub>2</sub>(B)@carbon composite nanowires as anode for lithium ion batteries with enhanced reversible capacity and cyclic performance. *J Mater Chem* 21(24):8591–8596

- [16] Cheng G, Wei Y, Xiong J et al (2017) Sorbitol-employed hydrothermal carbonization to TiO<sub>2</sub>@C mesoporous hybrids with promoted visible light utilization and excellent photo-sensitization stability. *J Alloys Compd* 723:948–959
- [17] Kang K-Y, Lee Y-G, Kim S et al (2012) Electrochemical properties of carbon-coated TiO<sub>2</sub> nanotubes as a lithium battery anode material. *Mater Chem Phys* 137(1):169–176
- [18] Shen J, Wang H, Song Y et al (2014) Amorphous carbon coated TiO<sub>2</sub> nanocrystals embedded in a carbonaceous matrix derived from polyvinylpyrrolidone decomposition for improved Li-storage performance. *Chem Eng J* 240:379–386
- [19] Cheng G, Stadler FJ (2015) Achieving phase transformation and structure control of crystalline anatase TiO<sub>2</sub>@C hybrids from titanium glycolate precursor and glucose molecules. *J Colloid Interface Sci* 438:169–178
- [20] Cheng G, Xu F, Xiong J et al (2016) Enhanced adsorption and photocatalysis capability of generally synthesized TiO<sub>2</sub>-carbon materials hybrids. *Adv Powder Technol* 27(5):1949–1962
- [21] Li Q, Liu B, Li Y et al (2009) Ethylene glycol-mediated synthesis of nanoporous anatase TiO<sub>2</sub> rods and rutile TiO<sub>2</sub> self-assembly chrysanthemums. *J Alloys Compd* 471(1–2):477–480
- [22] Gan Y, Zhu L, Qin H et al (2015) Hybrid nanoarchitecture of rutile TiO<sub>2</sub> nanoneedle/graphene for advanced lithium-ion batteries. *Solid State Ionics* 269:44–50
- [23] Zhao J, Liu Y, Fan M et al (2015) From solid-state metal alkoxides to nanostructured oxides: a precursor-directed synthetic route to functional inorganic nanomaterials. *Inorg Chem Front* 2(3):198–212
- [24] Das J, Freitas FS, Evans IR et al (2010) A facile nonaqueous route for fabricating titania nanorods and their viability in quasi-solid-state dye-sensitized solar cells. *J Mater Chem* 20(21):4425–4431
- [25] Zakharova GS, Andreikov EI, Osipova VA et al (2013) Effect of the titanium glycerolate precursor heat treatment procedure on the morphology and photocatalytic properties of TiO<sub>2</sub> nanopowder. *Inorg Mater* 49(11):1127–1132
- [26] Weirich TE, Winterer M, Seifried S et al (2000) Rietveld analysis of electron powder diffraction data from nanocrystalline anatase, TiO<sub>2</sub>. *Ultramicroscopy* 81(3–4):263–270
- [27] Gonschorek W (1982) X-ray charge density study of rutile (TiO<sub>2</sub>). *Z Kristallogr Cryst Mater* 160(1–4):187–204
- [28] Rouquerol J, Avnir D, Fairbridge CW et al (1994) Recommendations for the characterization of porous solids (Technical Report). *Pure Appl Chem* 66(8):1739–1758
- [29] Preiss H, Berger L-M, Schultze D (1999) Studies on the carbothermal preparation of titanium carbide from different gel precursors. *J Eur Ceram Soc* 19(2):195–206
- [30] Taziwa R, Meyer EL, Chinyama KG (2012) Raman temperature dependence analysis of carbon-doped titanium dioxide nanoparticles synthesized by ultrasonic spray pyrolysis technique. *J Mater Sci* 47(3):1531–1540. <https://doi.org/10.1007/s10853-011-5943-4>
- [31] Balachandran U, Eror NG (1982) Raman spectra of titanium dioxide. *J Solid State Chem* 42(3):276–282
- [32] Zhang H, Li F, Jia Q et al (2008) Preparation of titanium carbide powders by sol-gel and microwave carbothermal reduction methods at low temperature. *J Sol-Gel Sci Technol* 46(2):217–222
- [33] Ohzuku T, Kodama T, Hirai T (1985) Electrochemistry of anatase titanium dioxide in lithium nonaqueous cells. *J Power Sources* 14(1–3):153–166
- [34] Wagemaker M, van de Krol R, Kentgens APM et al (2001) Two phase morphology limits lithium diffusion in TiO<sub>2</sub> (anatase): a <sup>7</sup>Li MAS NMR study. *J Am Chem Soc* 123(46):11454–11461
- [35] Subramanian V, Karki A, Gnanasekar KI et al (2006) Nanocrystalline TiO<sub>2</sub> (anatase) for Li-ion batteries. *J Power Sources* 159(1):186–192
- [36] Reddy MA, Kishore MS, Pralong V et al (2006) Room temperature synthesis and Li insertion into nanocrystalline rutile TiO<sub>2</sub>. *Electrochem Commun* 8(8):1299–1303
- [37] Kubiak P, Pfanzelt M, Geserick J et al (2009) Electrochemical evaluation of rutile TiO<sub>2</sub> nanoparticles as negative electrode for Li-ion batteries. *J Power Sources* 194(2):1099–1104
- [38] Verma P, Maire P, Novák P (2010) A review of the features and analyses of the solid electrolyte interphase in Li-ion batteries. *Electrochim Acta* 55(22):6332–6341
- [39] Dahn JR, Sleight AK, Shi H et al (1993) Dependence of the electrochemical intercalation of lithium in carbons on the crystal structure of the carbon. *Electrochim Acta* 38(9):1179–1191
- [40] Borghols WJH, Lützenkirchen-Hecht D, Haake U et al (2010) Lithium Storage in Amorphous TiO<sub>2</sub> Nanoparticles. *J Electrochem Soc* 157(5):A582–A588
- [41] Guo Y-G, Hu Y-S, Maier J (2006) Synthesis of hierarchically mesoporous anatase spheres and their application in lithium batteries. *Chem Commun* 417(26):2783–2785
- [42] Chen Z, Yuan Y, Zhou H et al (2014) 3D nanocomposite architectures from carbon-nanotube-threaded nanocrystals for high-performance electrochemical energy storage. *Adv Mater* 26(2):339–345
- [43] Shin J-Y, Samuelis D, Maier J (2011) Sustained lithium-storage performance of hierarchical, nanoporous anatase TiO<sub>2</sub> at high rates: emphasis on interfacial storage phenomena. *Adv Funct Mater* 21(18):3464–3472

- [44] Kim C, Buonsanti R, Yaylian R et al (2013) Carbon-free TiO<sub>2</sub> battery electrodes enabled by morphological control at the nanoscale. *Adv Energy Mater* 3(10):1286–1291
- [45] Liu H, Li W, Shen D et al (2015) Graphitic Carbon Conformal Coating of Mesoporous TiO<sub>2</sub> Hollow Spheres for High-Performance Lithium Ion Battery Anodes. *J Am Chem Soc* 137(40):13161–13166
- [46] Yang Y, Ji X, Jing M et al (2015) Carbon dots supported upon N-doped TiO<sub>2</sub> nanorods applied into sodium and lithium ion batteries. *J Mater Chem A* 3(10):5648–5655
- [47] Xiu Z, Hao X, Wu Y et al (2015) Graphene-bonded and -encapsulated mesoporous TiO<sub>2</sub> microspheres as a high-performance anode material for lithium ion batteries. *J Power Sources* 287:334–340